STAR FORMATION

A far-ultraviolet–driven photoevaporation flow observed in a protoplanetary disk

Olivier Berné[1]*, Emilie Habart[2], Els Peeters[3,4,5], Ilane Schroetter[1], Amélie Canin[1], Ameek Sidhu[3,4], Ryan Chown[3,4], Emeric Bron[6], Thomas J. Haworth[7], Pamela Klaassen[8], Boris Trahin[2], Dries Van De Putte[9], Felipe Alarcón[10], Marion Zannese[2], Alain Abergel[2], Edwin A. Bergin[10], Jeronimo Bernard-Salas[11,12], Christiaan Boersma[13], Jan Cami[3,4,5], Sara Cuadrado[14], Emmanuel Dartois[15], Daniel Dicken[2], Meriem Elyaouri[2], Asunción Fuente[16], Javier R. Goicoechea[14], Karl D. Gordon[9,17], Lina Issa[1], Christine Joblin[1], Olga Kannavou[2], Baria Khan[3], Ozan Lacinbala[2], David Languignon[6], Romane Le Gal[1,18,19], Alexandros Maragkoudakis[13], Raphael Meshaka[2], Yoko Okada[20], Takashi Onaka[21,22], Sofia Pasquini[3], Marc W. Pound[23], Massimo Robberto[9,17], Markus Röllig[20], Bethany Schefter[3], Thiébaut Schirmer[2,24], Thomas Simmer[2], Benoit Tabone[2], Alexander G. G. M. Tielens[23,25], Sílvia Vicente[26], Mark G. Wolfire[23], PDRs4All Team†

Most low-mass stars form in stellar clusters that also contain massive stars, which are sources of far-ultraviolet (FUV) radiation. Theoretical models predict that this FUV radiation produces photodissociation regions (PDRs) on the surfaces of protoplanetary disks around low-mass stars, which affects planet formation within the disks. We report James Webb Space Telescope and Atacama Large Millimeter Array observations of a FUV-irradiated protoplanetary disk in the Orion Nebula. Emission lines are detected from the PDR; modeling their kinematics and excitation allowed us to constrain the physical conditions within the gas. We quantified the mass-loss rate induced by the FUV irradiation and found that it is sufficient to remove gas from the disk in less than a million years. This is rapid enough to affect giant planet formation in the disk.

Young low-mass stars are surrounded by protoplanetary disks of gas and dust, which have lifetimes of a few million years (*1*–*3*) and are the sites of planet formation (*4*). Planet formation is limited by processes that remove mass from the disk, such as photoevaporation (*5*). This occurs when the upper layers of protoplanetary disks are heated by x-ray or ultraviolet photons. Radiative heating increases the gas temperature, which brings the local sound speed above the escape velocity of the disk, causing the gas to escape from the system. Those photons could be from the central star (*6*) or from nearby massive stars (*7*). Because most low-mass stars form in clusters that also contain massive stars, most protoplanetary disks are exposed to external radiation, and so they are expected to experience photoevaporation driven by ultraviolet photons during their lifetime (*7*–*11*). Theoretical models predict that far-ultraviolet (FUV) photons, those with energies below the Lyman limit (energy E < 13.6 eV), dominate the photoevaporation process. The effect affects the disk mass, radius, and lifetime (*7*, *10*, *12*–*18*); its chemical evolution (*19*–*21*); and the growth and migration of any planets forming within the disk (*22*). However, these processes have not been directly observed.

Most observational constraints on the mass-loss rates associated with photoionization have been obtained for objects in the Orion Nebula known as proplyds, in which the ionization of FUV-driven photoevaporation flows from disks produces comet-shaped ionization fronts (*23*, *24*). Modeling of the observed ionization fronts of proplyds has indicated mass-loss rates $\dot{M} \approx 10^{-8}$ to 10^{-6} solar masses per year ($M_\odot$ year^{-1}) (*25*–*27*). However, those observations did not determine the physical conditions (radiation field, gas temperature, and density) at the locations where the photoevaporation flows are launched. In the regions where FUV photons penetrate the disk, a photodissociation region (PDR) (*28*) forms at the disk surface. Most observational tracers of PDR physics (spectral lines of H_2, O, and C^+) are in the near- and far-infrared wavelength ranges. The spatial scale of PDRs in externally illuminated disks is a few hundred astronomical units (au), which corresponds to angular sizes <1 arc sec (″) for the closest star-forming clusters (*12*, *29*, *30*).

Images of a photoevaporation flow

Figure 1 shows optical and near-infrared images of the Orion Bar, a ridge in the Orion Nebula (*31*) situated about 0.25 pc southeast of the Trapezium Cluster of massive stars. The western edge of the bar constitutes the ionization front (Fig. 1B), which separates regions where the gas is fully ionized and at temperature $T \sim 10^4$ K from the neutral atomic region at $T \sim 500$ to 1000 K. We investigated the source [BOM2000] d203-506 (hereafter d203-506) (*32*, *33*), a protoplanetary disk seen in absorption against the bright background, which is located at the following coordinates: right ascension $5^h35^m20^s.357$ and declination −5°25′05″.81 (J2000 equinox). Previous observations of d203-506 found no sign of an ionization front (*32*–*34*), indicating that the radiation field reaching the disk is dominated by FUV photons.

We obtained near-infrared and submillimeter observations of d203-506, with the James Webb Space Telescope (JWST) and the Atacama Large Millimeter Array (ALMA), respectively, both at angular resolution ~0.1″ (corresponding to ~40 au at the distance of the Orion Nebula). JWST images were taken in multiple broad and narrow band filters using the Near-Infrared Camera (NIRCam) instrument (*35*). We also obtained near-infrared spectroscopic observations using the integral field unit (IFU) of the Near-Infrared Spectrograph (NIRSpec) instrument on JWST (*35*). The ALMA interferometric data cubes provided maps of rotational emission lines from the molecules HCN and HCO^+, with a velocity resolution of 0.2 km s^{-1} (*35*).

Figure 2 compares the JWST and ALMA images to archival optical images from the Hubble

[1]Institut de Recherche en Astrophysique et Planétologie, Université de Toulouse, Centre National de la Recherche Scientifique (CNRS), Centre National d'Etudes Spatiales, 31028 Toulouse, France. [2]Institut d'Astrophysique Spatiale, Université Paris-Saclay, CNRS, 91405 Orsay, France. [3]Department of Physics and Astronomy, The University of Western Ontario, London, ON N6A 3K7, Canada. [4]Institute for Earth and Space Exploration, The University of Western Ontario, London, ON N6A 3K7, Canada. [5]Carl Sagan Center, Search for ExtraTerrestrial Intelligence Institute, Mountain View, CA 94043, USA. [6]Laboratoire d'Etudes du Rayonnement et de la Matière, Observatoire de Paris, Université Paris Science et Lettres, CNRS, Sorbonne Universités, F-92190 Meudon, France. [7]School of Physics and Astronomy, Queen Mary University of London, London E1 4NS, UK. [8]UK Astronomy Technology Centre, Royal Observatory Edinburgh, Blackford Hill EH9 3HJ, UK. [9]Space Telescope Science Institute, Baltimore, MD 21218, USA. [10]Department of Astronomy, University of Michigan, Ann Arbor, MI 48109, USA. [11]ACRI-ST, Centre d'Etudes et de Recherche de Grasse, F-06130 Grasse, France. [12]Innovative Common Laboratory for Space Spectroscopy, 06130 Grasse, France. [13]NASA Ames Research Center, Moffett Field, CA 94035, USA. [14]Instituto de Física Fundamental, Consejo Superior de Investigaciones Científicas, 28006 Madrid, Spain. [15]Institut des Sciences Moléculaires d'Orsay, Université Paris-Saclay, CNRS, 91405 Orsay, France. [16]Centro de Astrobiología, Consejo Superior de Investigaciones Científicas, and Instituto Nacional de Técnica Aeroespacial, 28850 Torrejón de Ardoz, Spain. [17]Johns Hopkins University, Baltimore, MD 21218, USA. [18]Institut de Planétologie et d'Astrophysique de Grenoble, Université Grenoble Alpes, CNRS, F-38000 Grenoble, France. [19]Institut de Radioastronomie Millimétrique, F-38406 Saint-Martin d'Hères, France. [20]I. Physikalisches Institut, Universität zu Köln, 50937 Köln, Germany. [21]Department of Astronomy, Graduate School of Science, The University of Tokyo, Tokyo 113-0033, Japan. [22]Department of Physics, Faculty of Science and Engineering, Meisei University, Hino, Tokyo 191-8506, Japan. [23]Astronomy Department, University of Maryland, College Park, MD 20742, USA. [24]Department of Space, Earth and Environment, Chalmers University of Technology, Onsala Space Observatory, SE-439 92 Onsala, Sweden. [25]Leiden Observatory, Leiden University, 2300 RA Leiden, Netherlands. [26]Instituto de Astrofísica e Ciências do Espaço, P-1349-018 Lisboa, Portugal.
*Corresponding author. Email: olivier.berne@irap.omp.eu
†PDRs4All Team authors and affiliations are listed in the supplementary materials.

Space Telescope (HST). The nearly edge-on (*35*) dusty disk of d203-506 is visible in absorption in all the HST and JWST images (Fig. 2, A to F) but in emission in the 344-GHz (870 μm) dust continuum (Fig. 2G). It is also seen in emission with ALMA in Fig. 2H, which shows the HCN ($v = 0, J = 4 \rightarrow 3$) line, where v and J denote the vibrational and rotational quantum numbers, respectively, at 354.505 GHz (845.664 μm), which traces cold molecular gas. Figure 2, I and E, shows emission maps of ALMA HCO^+ ($v = 0, J = 4 \rightarrow 3$) at 356.734 GHz (840.381 μm) and NIRCam H_2 ($v = 1 \rightarrow 0, J = 3 \rightarrow 1$) at 2.12 μm, respectively, which both show emission from the PDR surrounding the disk and absorption at the center. Both the H_2 rovibrational and HCO^+ rotational emission lines trace warm (gas kinetic temperatures T_{gas} ~ 500 to 1000 K)

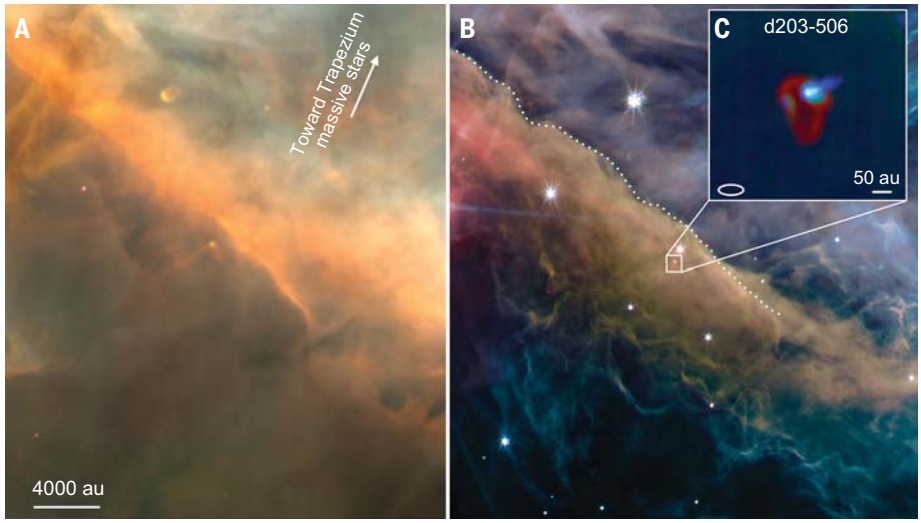

Fig. 1. Optical and near-infared images of the Orion Bar region. (**A**) HST optical image centered at coordinates right ascension $5^h35^m20^s.183$ and declination −5°25′06″.14. [O III] filter at 502 nm is in blue, Hα filter at 656 nm is in green, and [N II] filter at 658 nm is in red. [Credit: NASA/STScI/Rice University/C. O'Dell *et al.* (*47*)]. (**B**) JWST near-infrared image of the same region at the same scale. Filters centered at 1.4 and 2.0 μm are in blue; at 2.77, 3.00, 3.23, 3.35, and 3.32 μm in green; at 4.05 μm in orange; and at 4.44, 4.80, and 4.70 μm in red. In (A) and (B), the Orion Bar separates regions where the gas is fully ionized (upper right) from those where it is in neutral form (lower left). (**C**) Zoomed-in view of the d203-506 disk. Red is the NIRCam image in the 2.12-μm filter, which traces molecular hydrogen; blue is the 1.64-μm filter, which traces [Fe II] emission lines; and green is the emission in the 1.40-μm broad-band filter, which traces scattered light.

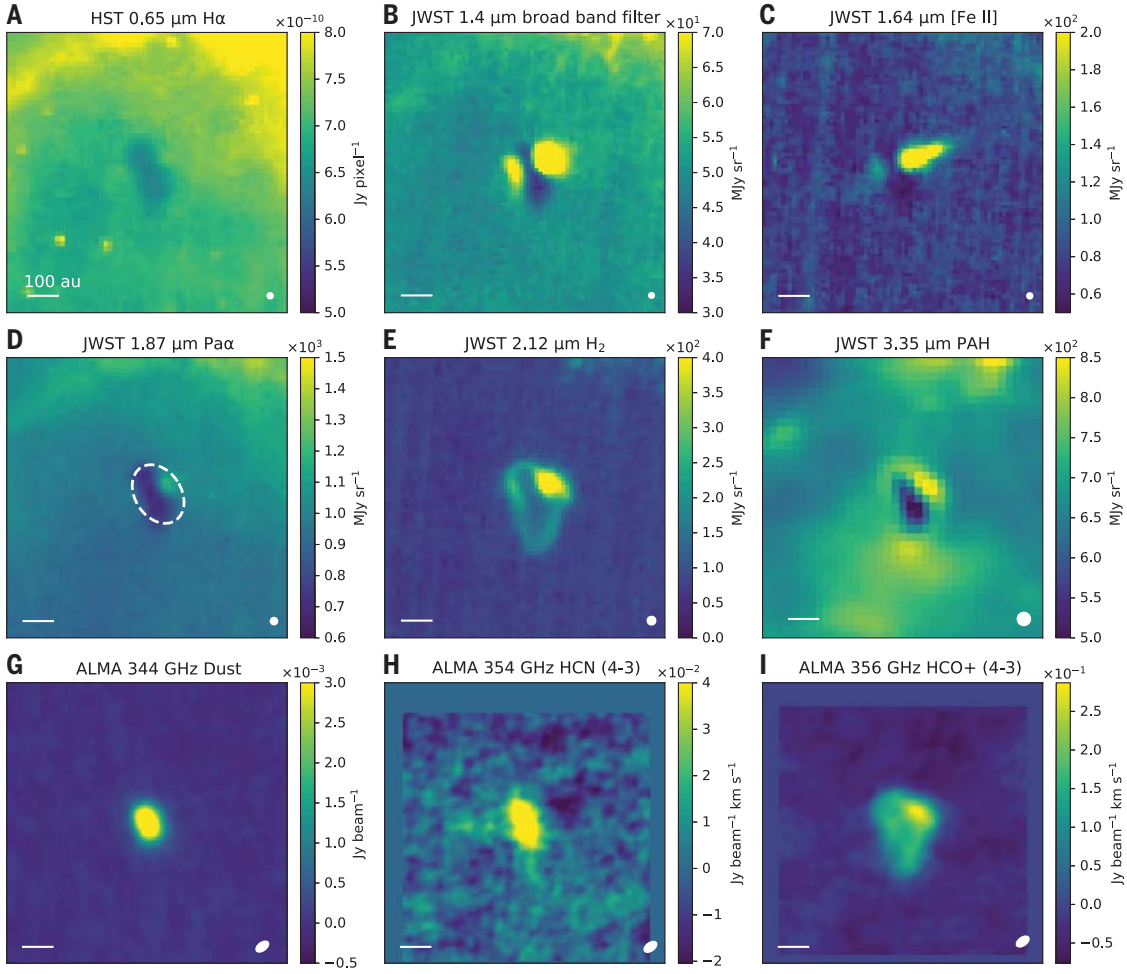

Fig. 2. Multiwavelength images of the d203-506 disk. (**A**) HST optical image in a Hα filter (*23*). (**B** to **F**) JWST near-infrared images (*35*). [(E) is reproduced with permission from (*33*)]. (**G** to **I**) ALMA submillimeter images (*35*). In all panels, the white-filled ellipse indicates the size and shape of the point spread function or reconstructed telescope beam, and the horizontal bar is 100 au. The white-dashed ellipse in (D) indicates the shape of the aperture used for the extraction of the NIRSpec spectrum in Fig. 4. The wavelength and physical assignment of each image is labeled above each panel; in (H) and (I), (4-3) is an abbreviation of ($v = 0, J = 4 \rightarrow 3$). 1 Jy = 1×10^{-26} Wm^{-2} Hz^{-1}.

molecular gas in PDRs (*31*). The PDR is also bright in the 3.35-μm NIRCam filter (Fig. 2F), which is dominated by aromatic infrared band (AIB) emission from ultraviolet-excited polycyclic aromatic hydrocarbon (PAH) molecules. PAHs are known to be tracers of PDRs (*36*) and have been previously mapped in a proplyd in the Orion Nebula (*37*). The PDR in d203-506 is spatially resolved and extends south from the disk, forming a lobe shape. A jet is visible in the NIRCam [Fe II] filter at 1.62 μm (Fig. 2C). A bright emission spot is present in the H_2 and HCO^+ images in the northwestern part of the PDR and is also visible in the broad-band filter at 1.4 μm (Fig. 2B). The location of this bright spot coincides with the region of interaction between the jet and the PDR, which is visible only on the side facing the Trapezium Cluster. There is also AIB emission in the 3.35-μm NIRCam filter at this location (Fig. 2F), which indicates ultraviolet excitation. Figure 3 shows a schematic diagram of our interpretation of the morphological features in d203-506.

Physical properties of the PDR

Figure 4 shows the NIRSpec spectrum of d203-506 (*35*). Numerous rovibrational emission lines of CO ($v = 1 \rightarrow 0$ and $v = 2 \rightarrow 1$), OH ($v = 1 \rightarrow 0$), CH^+ ($v = 1 \rightarrow 0$), and H_2 (up to $J = 15$) are detected. We interpreted these lines as coming from the PDR, so we traced the physical conditions of gas in that region. We modeled (*35*) the H_2 lines using the Meudon PDR code (*38*), which calculates the H_2 excitation in PDRs (Fig. 5). We derived the hydrogen number density n_H and temperature of the gas in the H_2 emitting layer (compare with Figure 2E) as $n_H = 5.5 \times 10^5$ to 1.0×10^7 cm^{-3} and $T_{gas} = 1240$ to 1260 K.

We fitted a Keplerian orbit model to the HCN emission map (fig. S2) and used it to set an upper limit on the mass of d203-506's central star $M_* < 0.3\,M_\odot$ (*35*). Taking $T_{gas} \sim 1250$ K as determined above, the speed of sound $c_S \equiv \sqrt{\frac{7/5 k_B T_{gas}}{\mu m_H}} = 3.3$ km s^{-1}, where k_B is the Boltzmann constant, m_H is the mass of the hydrogen atom, and μ is the ratio of total mass to hydrogen mass of the gas, which we assume equals the interstellar value [μ = 1.4 (*39*)].

This value of c_S exceeds the escape velocity at distances from the central star above a critical value, defined as the gravitational radius $r_g \equiv \frac{GM_*}{c_S^2}$ (*40*), where G is Newton's gravitational constant. For $M_* < 0.3\,M_\odot$ and $T_{gas} \sim 1250$ K, we found $r_g < 26$ au. This is much smaller than the observed radial extent of the H_2 emission $r_{H_2} = 132 \pm 13$ au [and its height $h_{H_2} = 56 \pm 13$ au (*35*)]. Therefore, the gas in this layer is not gravitationally bound and flows outward from the disk, at roughly the speed of sound. The associated mass flux through the PDR is $j = \mu m_H n_H c_S$, and the total mass loss rate is $\dot{M} = j \times S$, where S is the surface area of the H_2-emitting layer (*35*). Including the uncertainties on r_{H_2}, h_{H_2}, n_H, and T_{gas} (table S1), we calculated $\dot{M} = 1.4 \times 10^{-7}$ to 4.6×10^{-6} $M_\odot$ year^{-1}.

We also investigated an alternative method of determining the mass-loss rate, using 1D dynamical models, and found a consistent value of $\dot{M}$ (*35*). All the physical quantities that we derived are listed in table S1.

Implications for planet formation

Gas in protoplanetary disks is the raw material from which giant planets form, so mass loss due to photoevaporation can limit the formation of such planets. The effects of FUV radiation depend on the stellar mass, which sets the strength of the gravitational field that acts to retain the gas.

Theoretical models of planet growth under the influence of external FUV photoevaporation have predicted that FUV radiation fields with intensity $G_0 \gtrsim 500$ [where G_0 is the ratio of the ultraviolet radiation field to the average value in the interstellar medium (*41*)] suppress giant planet formation around stars with masses $\lesssim 0.5\,M_\odot$ (*22*). Our results for d203-506 are consistent with this prediction: We found that $M_* < 0.3\,M_\odot$ and the radiation field is $G_0 \lesssim 10^5$ (*35*), whereas the mass-loss rate $\dot{M} = 1.4 \times 10^{-7}$ to 4.6×10^{-6} $M_\odot$ year^{-1} implies a disk depletion timescale $\tau \equiv M_d/\dot{M} <$ 0.13 million years, where M_d is the disk mass

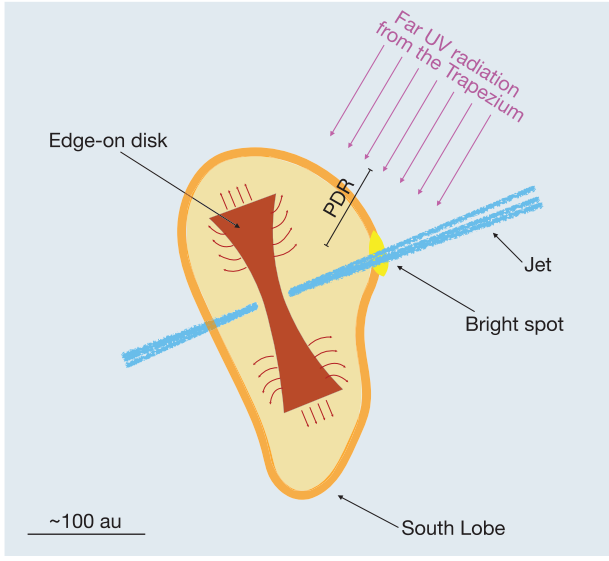

Fig. 3. Schematic diagram of our interpretation of d203-506. Dark brown is the edge-on disk of cold molecular gas, which appears in absorption in the NIRCam images but in emission in the ALMA HCN and dust continuum images (Fig. 2). Brown arrows indicate molecular gas escaping from this disk, which feeds the photoevaporation flow. This produces an envelope around the disk (light brown shading), which is delimited by the dissociation front (orange band), where molecular hydrogen is dissociated into hydrogen atoms by FUV photons (pink arrows) coming from the Trapezium Cluster. The transition from molecular gas in the disk to atomic gas under ultraviolet irradiation constitutes the PDR. Blue shows the jet from the central star, which corresponds to the [Fe II] emission (Fig. 2C). The jet interacts with the envelope, producing a bright emission spot (yellow). The surroundings of d203-506 (gray) consist of diffuse atomic gas.

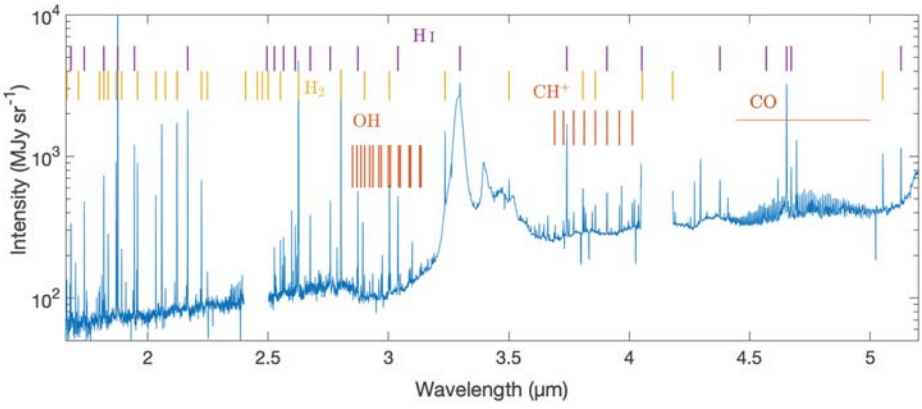

Fig. 4. JWST NIRSpec spectrum of d203-506. Colored tick marks indicate detected species, as labeled. The broad emission bands at 3.3 and 3.4 μm are C-H vibrational emission from PAH molecules. Other unlabeled lines are mostly atomic (e.g., [O I] or [Fe II]). There are no data at wavelengths 2.40 to 2.50 μm and 4.05 to 4.18 μm owing to gaps in the NIRSpec detectors.

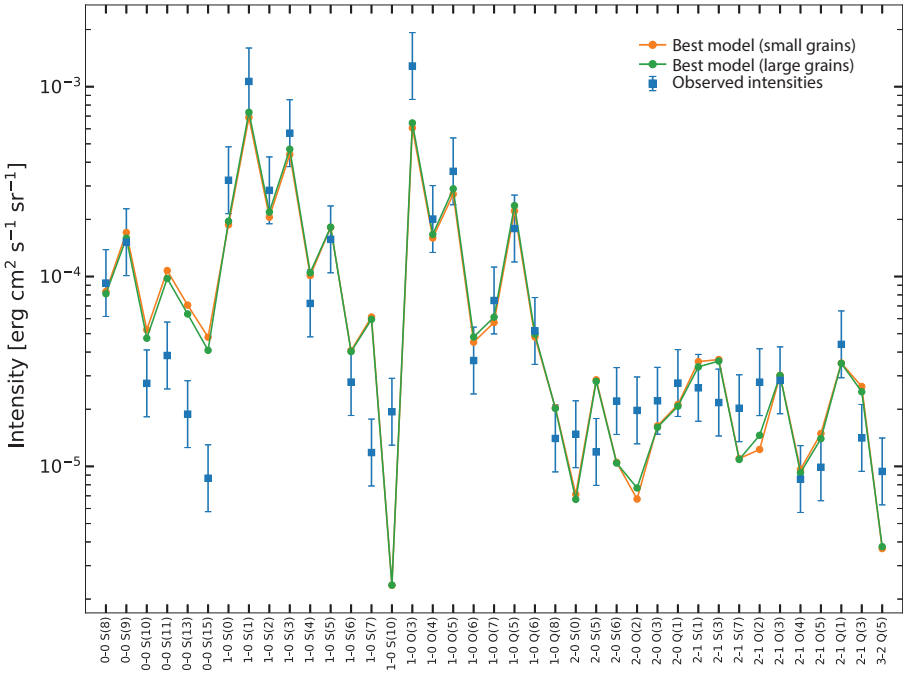

Fig. 5. Observed and modeled H_2. Line intensities for d203-506. Blue squares show the observed line intensities (table S2), with error bars enclosing 50% uncertainty, estimated from the χ^2 (*35*). The instrumental uncertainties are smaller than the symbols. Colored lines are the best-fitting models (*35*) using small dust grains (orange) or large dust grains (green); circles show the model intensities of each line. H_2 line identifications are abbreviated; the full quantum levels corresponding to this notation are listed in table S2.

(*35*). This is faster than even very early planet formation (*42*, *43*).

A positive correlation has been observed between stellar mass and the frequency of Jupiter-mass exoplanets orbiting those stars (*44*, *45*), which we suggest could be due to FUV radiation in stellar clusters during the planet formation process. Dynamical and compositional studies of the Solar System indicate that it formed in a stellar cluster that contained one or more massive stars (*46*), and so it might have been affected by FUV radiation.

REFERENCES AND NOTES

1. J. P. Williams, L. A. Cieza, *Annu. Rev. Astron. Astrophys.* **49**, 67–117 (2011).
2. K. E. Haisch Jr., E. A. Lada, C. J. Lada, *Astrophys. J.* **553**, L153–L156 (2001).
3. S. M. Andrews, *Annu. Rev. Astron. Astrophys.* **58**, 483–528 (2020).
4. M. Keppler *et al.*, *Astron. Astrophys.* **617**, A44 (2018).
5. U. Gorti, R. Liseau, Z. Sándor, C. Clarke, *Space Sci. Rev.* **205**, 125–152 (2016).
6. U. Gorti, D. Hollenbach, *Astrophys. J.* **690**, 1539–1552 (2008).
7. F. C. Adams, D. Hollenbach, G. Laughlin, U. Gorti, *Astrophys. J.* **611**, 360–379 (2004).
8. C. J. Lada, E. A. Lada, *Annu. Rev. Astron. Astrophys.* **41**, 57–115 (2003).
9. M. Fatuzzo, F. C. Adams, *Astrophys. J.* **675**, 1361–1374 (2008).
10. A. J. Winter, J. D. Kruijssen, M. Chevance, B. W. Keller, S. N. Longmore, *Mon. Not. R. Astron. Soc.* **491**, 903–922 (2020).
11. A. J. Winter, T. J. Haworth, *Eur. Phys. J. Plus* **137**, 1132 (2022).
12. H. Störzer, D. Hollenbach, *Astrophys. J.* **515**, 669–684 (1999).
13. A. Scally, C. Clarke, *Mon. Not. R. Astron. Soc.* **325**, 449–456 (2001).
14. C. J. Clarke, *Mon. Not. R. Astron. Soc.* **376**, 1350–1356 (2007).
15. F. Concha-Ramírez, M. J. C. Wilhelm, S. Portegies Zwart, T. J. Haworth, *Mon. Not. R. Astron. Soc.* **490**, 5678–5690 (2019).
16. A. J. Winter *et al.*, *Mon. Not. R. Astron. Soc.* **478**, 2700–2722 (2018).
17. R. B. Nicholson *et al.*, *Mon. Not. R. Astron. Soc.* **485**, 4893–4905 (2019).
18. G. A. L. Coleman, T. J. Haworth, *Mon. Not. R. Astron. Soc.* **514**, 2315–2332 (2022).
19. C. Walsh, T. J. Millar, H. Nomura, *Astrophys. J. Lett.* **766**, L23 (2013).
20. T. J. Haworth, *Mon. Not. R. Astron. Soc.* **503**, 4172–4182 (2021).
21. R. D. Boyden, J. A. Eisner, *Astrophys. J.* **947**, 7 (2023).
22. A. J. Winter, T. J. Haworth, G. A. Coleman, S. Nayakshin, *Mon. Not. R. Astron. Soc.* **515**, 4287–4301 (2022).
23. C. R. O'Dell, Z. Wen, *Astrophys. J.* **436**, 194 (1994).
24. C. R. O'Dell, *Astron. J.* **115**, 263–273 (1998).
25. D. Johnstone, D. Hollenbach, J. Bally, *Astrophys. J.* **499**, 758–776 (1998).
26. W. Henney, S. Arthur, *Astron. J.* **116**, 322–335 (1998).
27. W. J. Henney, C. R. O'Dell, *Astron. J.* **118**, 2350–2368 (1999).
28. A. Tielens, D. Hollenbach, *Astrophys. J.* **291**, 722 (1985).
29. H. Chen *et al.*, *Astrophys. J.* **492**, L173–L176 (1998).
30. J. Champion *et al.*, *Astron. Astrophys.* **604**, A69 (2017).
31. J. R. Goicoechea *et al.*, *Nature* **537**, 207–209 (2016).
32. J. Bally, C. R. O'Dell, M. J. McCaughrean, *Astron. J.* **119**, 2919–2959 (2000).
33. O. Berné *et al.*, *Nature* **621**, 56–59 (2023).
34. E. Habart *et al.*, *Astron. Astrophys.* **673**, A149 (2023).
35. Materials and methods are available as supplementary materials.
36. E. Peeters *et al.*, *Astron. Astrophys.* **390**, 1089–1113 (2002).
37. S. Vicente *et al.*, *Astrophys. J. Lett.* **765**, L38 (2013).
38. F. Le Petit, C. Nehme, J. Le Bourlot, E. Roueff, *Astrophys. J. Suppl. Ser.* **164**, 506–529 (2006).
39. B. T. Draine, *Physics of the Interstellar and Intergalactic Medium* (Princeton Univ. Press, 2011).
40. D. Hollenbach, D. Johnstone, S. Lizano, F. Shu, *Astrophys. J.* **428**, 654 (1994).
41. H. J. Habing, *Bull. Astron. Inst. Neth.* **19**, 421 (1968).
42. A. Stolte *et al.*, *Astron. Astrophys.* **578**, A4 (2015).
43. P. D. Sheehan, J. A. Eisner, *Astrophys. J.* **857**, 18 (2018).
44. J. A. Johnson, K. M. Aller, A. W. Howard, J. R. Crepp, *Publ. Astron. Soc. Pac.* **122**, 905–915 (2010).
45. S. Reffert, C. Bergmann, A. Quirrenbach, T. Trifonov, A. Künstler, *Astron. Astrophys.* **574**, A116 (2015).
46. E. A. Bergin, C. Alexander, M. Drozdovskaya, M. Gounelle, S. Pfalzner, arXiv:2301.05212 [astro-ph.EP] (2023).
47. NASA Hubblesite, Star Factory at the Center of the Orion Nebula, Space Telescope Science Institute (2005); https://hubblesite.org/contents/media/images/2005/12/1674-Image.html.
48. J. Champion, ALMA cubes and integrated maps of the d203-506 protoplanetary disk. Zenodo (2023); https://doi.org/10.5281/zenodo.8196030.
49. I. Schroetter, JWST NIRSpec spectrum of the d203-506 protoplanetary disk. Zenodo (2023); https://doi.org/10.5281/zenodo.10260214.
50. The Meudon PDR Team, Meudon PDR Code, version used for Berné et al. Science 2024. Zenodo (2023); https://doi.org/10.5281/zenodo.10488834.

ACKNOWLEDGMENTS

We thank the anonymous referees for helpful feedback and comments and C. O'Dell for providing comments. The JWST helpdesk provided support with data reduction. Part of this work used the DiRAC Data Intensive service at Leicester, operated by the University of Leicester IT Services, which forms part of the STFC DiRAC HPC Facility. **Funding:** A.F. thanks the Spanish MICIN for funding support from grant PID2019-106235GB-I00. O.B., I.S., and A.C. are funded by the Centre National d'Etudes Spatiales (CNES) through the APR program. J.R.G. and S.C. thank the Spanish MCINN for funding support under grant PID2019-106110GB-I00. P. Guillard thanks the University Pierre and Marie Curie, the Institut Universitaire de France, the CNES, the Programme National de Cosmologie and Galaxies (PNCG), and the Physique Chimie du Milieu Interstellaire (PCMI) programs of Centre National de la Recherche Scientifique/INSU for financial support. E.P. and J.C. acknowledge support from the Institute for Earth and Space Exploration, the Canadian Space Agency, and the Natural Sciences and Engineering Research Council of Canada. C.B. acknowledges funding from the San José State University Research Foundation (grant 80NSSC22M0107) and the Internal Scientist Funding Model (ISFM) Laboratory Astrophysics Directed Work Package at NASA Ames. T.O. is supported by JSPS Bilateral Program grant 120219939. T.J.H. is funded by a Royal Society Dorothy Hodgkin Fellowship. A.F. was supported by the Spanish program Unidad de Excelencia María de Maeztu CEX2020-001058-M, financed by grant MCIN/AEI/10.13039/501100011033. NN is funded through UAEU Program for Advanced Research (UPAR) grant G00003479. Y. Zhang is funded by the National Science Foundation of China (NSFC) grant 11973099 and the China Manned Space Project grants CMS-CSST-2021-A09 and -A10. M. Rö and Y.O. are supported by the Collaborative Research Centre 956, sub-project C1, funded by the Deutsche Forschungsgemeinschaft (DFG) project ID 184018867. P. Merino acknowledges grants EUR2021-122006, TED2021-129416A-I00 and PID2021-125309OA-I00 funded by MCIN/AEI/10.13039/501100011033 and European Union NextGenerationEU/PRTR. A. Pathak acknowledges financial support from the Department of Science and Technology Core Research Grant (DST-CRG) SERB-CRG/2021/000907, and the Institutes of Eminence (IoE) grant BHU incentive/2021-22/32439. M. Buragohain acknowledges a DST INSPIRE Faculty fellowship. J. He is sponsored by the Chinese Academy of Sciences (CAS), through a grant to the CAS South America Center for Astronomy (CASSACA) in Santiago, Chile. H. Zettergren acknowledges support from the Swedish Research Council contract 2020-03437. **Author contributions:** O.B., E.H., and E.P. led the JWST observing program. O.B. led the study and drafted the manuscript and produced Figs. 1, 3, and 4 and figs. S1, S3, and S4. E. B. and F.L.P. produced the PDR models and Fig. 5 and figs. S4 to S6. T.J.H. produced the 1D dynamical models and fig. S7. F.A. produced the disk 3D radiative transfer models and fig. S2. A. Canin produced Fig. 2. J. Champion was principal investigator of the ALMA observing program. J. Champion and E. Chapillon performed the ALMA data reduction. P.K. analyzed the ALMA data. I.S., A.S., R.C., D.V.D.P., and F.A. reduced the NIRSpec data. A.C. and B.Tr. reduced the

NIRCam data. I.S. extracted the NIRSpec spectrum. I.S. and M.Z. measured the line intensities. M.Z. produced the LTE radiative transfer models of CH^+ and OH. J.C. provided the radiative transfer models for CO. All other authors contributed to the research presented in this paper or provided detailed feedback on the manuscript. All authors meet the journal's authorship requirements. **Competing interests:** The authors declare no competing interests. **Data and material availability:** The JWST and HST data are available on the MAST portal http://mast.stsci.edu under the proposal IDs 1288 and 6603, respectively. The ALMA raw data are available on the ALMA archive at https://almascience.eso.org/aq under project code 2017.1.01478.S. Our reduced ALMA data cubes and maps are archived at Zenodo (*48*), as is our reduced NIRSPec spectrum of d203-506 (*49*). The modified Meudon PDR code used in this paper is available at Zenodo (*50*).

SUPPLEMENTARY MATERIALS

science.org/doi/10.1126/science.adh2861
PDRs4All Team Authors and Affiliations
Materials and Methods
Figs. S1 to S7
Tables S1 and S2
References (*51*–*78*)

Submitted 24 February 2023; accepted 12 January 2024
10.1126/science.adh2861

NEUROSCIENCE

Touch sensation requires the mechanically gated ion channel ELKIN1

Sampurna Chakrabarti[1], Jasmin D. Klich[1], Mohammed A. Khallaf[1,2], Amy J. Hulme[3], Oscar Sánchez-Carranza[1], Zuzanna M. Baran[1,4], Alice Rossi[1], Angela Tzu-Lun Huang[1], Tobias Pohl[4], Raluca Fleischer[1], Carina Fürst[1,5], Annette Hammes[5], Valérie Bégay[1], Hanna Hörnberg[4,6], Rocio K. Finol-Urdaneta[3], Kate Poole[7], Mirella Dottori[3], Gary R. Lewin[1,8,9]*

Touch perception is enabled by mechanically activated ion channels, the opening of which excites cutaneous sensory endings to initiate sensation. In this study, we identify ELKIN1 as an ion channel likely gated by mechanical force, necessary for normal touch sensitivity in mice. Touch insensitivity in *Elkin1*$^{-/-}$ mice was caused by a loss of mechanically activated currents (MA currents) in around half of all sensory neurons activated by light touch (low-threshold mechanoreceptors). Reintroduction of *Elkin1* into sensory neurons from *Elkin1*$^{-/-}$ mice restored MA currents. Additionally, small interfering RNA–mediated knockdown of *ELKIN1* from induced human sensory neurons substantially reduced indentation-induced MA currents, supporting a conserved role for ELKIN1 in human touch. Our data identify ELKIN1 as a core component of touch transduction in mice and potentially in humans.

Touch sensation is fundamental to our sense of self, our social interactions, and our exploration of the tactile world (*1*, *2*). Sensation is initiated at specialized end organs in the skin, innervated by low-threshold mechanoreceptors (LTMRs) with their cell bodies in the dorsal root ganglia (DRGs). The peripheral endings of LTMRs are equipped with mechanically gated ion channels that can be opened by very small forces to initiate and enable touch perception (*3*, *4*). The mechanically gated ion channel PIEZO2 is expressed by most sensory neurons in the DRGs (*5*), and in the absence of PIEZO2, around half of LTMRs no longer respond to mechanical stimuli (*6*–*8*). The DRGs also contain so-called nociceptors, sensory neurons specialized to detect potentially damaging and painful stimuli, including intense mechanical force (*3*). Many nociceptors express PIEZO2 channels but remain mechanosensitive in its absence. The preservation of mechanosensitivity in many LTMRs in the absence of PIEZO2 channels (*6*–*8*) led us to search for other mechanically gated ion channels that could account for PIEZO2-independent sensory mechanotransduction.

[1]Molecular Physiology of Somatic Sensation Laboratory, Max Delbrück Center for Molecular Medicine in the Helmholtz Association (MDC), 13125 Berlin-Buch, Germany. [2]Department of Zoology and Entomology, Faculty of Science, Assiut University, Assiut 71516, Egypt. [3]School of Medical, Indigenous and Health Sciences, Molecular Horizons, University of Wollongong, Wollongong, NSW 2522, Australia. [4]Molecular and Cellular Basis of Behavior, Max Delbrück Center for Molecular Medicine in the Helmholtz Association (MDC), 13125 Berlin-Buch, Germany. [5]Molecular Pathways in Cortical Development, Max Delbrück Center for Molecular Medicine in the Helmholtz Association (MDC), 13125 Berlin-Buch, Germany. [6]NeuroCure Cluster of Excellence, Humboldt-Universität zu Berlin, 10117 Berlin, Germany. [7]School of Biomedical Sciences, Faculty of Medicine & Health, University of New South Wales, Sydney, NSW 2052, Australia. [8]Charité-Universitätsmedizin Berlin, 10117 Berlin, Germany. [9]German Center for Mental Health (DZPG), partner site Berlin, 10117 Berlin, Germany.
***Corresponding author. Email: glewin@mdc-berlin.de**

ELKIN1 can detect mechanical force

We previously identified ELKIN1 (TMEM87A) as a protein that is both necessary and sufficient to confer mechanosensitivity to highly metastatic human melanoma cells (*9*). Cryo–electron microscopy (cryo-EM) structures of human ELKIN1 recently revealed a monomeric seven-transmembrane protein with an N-terminal extracellular Golgi-dynamics domain fold (GOLD domain) (*10*). A second, higher-resolution structure recently identified a cation-conduction pathway through the protein (*11*). We overexpressed *Elkin1* in human embryonic kidney (HEK) 293T cells lacking PIEZO1 channels (HEK293T$^{Piezo1-/-}$ cells) (*12*) and found large indentation-induced mechanically activated currents (MA currents) in a majority of transfected cells (Fig. 1, A and B). Cells were plated on laminin 511 and poly-L-lysine (PLL), a substrate that supports increased mechanosensitivity (*13*); untransfected cells showed no indentation-induced currents. ELKIN1-dependent currents were rapidly-adapting (RA) with fast inactivation time constants (<10 ms), similar to those of PIEZO2 ion channels (*5*, *14*) (Fig. 1, A to C). Using substrate deflection by means of pillar arrays (*9*, *14*), we also found robust, mechanically activated currents in all HEK293T$^{Piezo1-/-}$ cells transfected with *Elkin1*-expression constructs, but also in cells transfected with *Elkin1* lacking the N-terminal GOLD-domain (*Elk1Δ170*) (Fig. 1, C and D, and fig. S1A) (*9*). Most of the pillar-evoked currents were RA (inactivation <10 ms) or intermediately adapting [(IA), inactivation between 10 and 50 ms]. Measurements of pillar-gated currents at different holding potentials revealed a linear current-voltage relationship with a reversal potential of 0 mV for both *Elkin1*- and *Elk1Δ170*-transfected cells (Fig. 1E). Therefore, our results suggest that the GOLD domain is not necessary for mechanical activation of ELKIN1. ELKIN1 currents showed a distinctive pharmacological profile, being sensitive to the nonspecific pore blocker Gd^{3+}(30 μM) but barely affected by ruthenium red (30 μM), a compound that completely blocks other mechanosensitive channels, such as PIEZO1 and PIEZO2 (*5*, *15*) (Fig. 1F and fig. S1B). Additionally, in agreement with recent reports (*11*, *15*), we found that cells expressing mouse *Elkin1* display prominent leak currents at very positive (>+60 mV) and very negative potentials (<−100 mV) (Fig. 1G and fig. S1C). ELKIN1 reconstituted into proteoliposomes reportedly show single-channel activity at very positive potentials (*16*). We also found that *Elkin1*-transfected HEK293T$^{Piezo1-/-}$ cells showed currents, which were substantially potentiated by application of mild positive-pressure pulses (20 mm of Hg) applied via the cell-attached pipette (fig. S2, A to C). Therefore, we provide multiple lines of evidence that ELKIN1 is likely an ion channel that can detect mechanical force.

Mouse sensory neurons express ELKIN1

We hypothesized that ELKIN1 could also be involved in mammalian touch sensation. We generated a CRISPR-Cas9–mediated genomic deletion of the mouse *Tmem87a/Elkin1* gene locus spanning sequences coding for transmembrane domains 2 to 6, which includes the